Journal of Environmental Chemical Engineering 10 (2022) 108790

Contents lists available at ScienceDirect

Journal of Environmental Chemical Engineering

journal homepage: www.elsevier.com/locate/jece

Graphitic carbon nitride thin films for light-induced photocatalysis in a slit geometry microreactor

Susmita Dolai [a,b,1], Anna Vanluchene [a,*,1], Petr Stavárek [a], Petr Dzik [c], Radek Fajgar [a], Karel Soukup [a], Petr Klusoň [a,b]

[a] Institute of Chemical Process Fundamentals of the Czech Academy of Sciences, Rozvojová 2/135, 165 02 Prague, Czech Republic
[b] Institute of Environmental Studies, Faculty of Science, Charles University, Benátská 2, 128 00 Prague, Czech Republic
[c] Institute of Physical and Applied Chemistry, Faculty of Chemistry, Brno University of Technology, Purkyňova 464/118, Královo Pole, 612 00 Brno, Czech Republic

ARTICLE INFO

Keywords:
Photochemistry
Photo-microreactor
Carbon nitride
Photocatalyst
Thin film

ABSTRACT

A combination of a photocatalysis and a micro-flow technology provides a highly capable tool for the design and utilisation of functional thin films. Here, they are represented by graphitic carbon nitride films, potentially used for photo-oxidations in environmental chemistry or for hydrogen evolution by water splitting. The optimised synthesis involves a study of the role of monomers, solvents, calcination temperatures, particle size, etc., in respect of the achieved photocatalytic activity. Films were prepared from the mixture of milled powder catalysts and a binder, dried, and subjected to post-processing treatments (post annealing, plasma application). The intended functionality was assessed in two types of reactions, photo-oxidation of a fluorescent dye, Rhodamine B, and photo-oxidation of a common antibiotic, Tetracycline. The performance was compared for the bulk catalyst, and for the thin film. In either case, the same part of light spectrum, concentrations, and other conditions were applied. However, for the thin films, a special experimental setup was utilised. It had the appearance of a micro-flow apparatus designed as a slit geometry photo-microreactor. Comparison of the two different reaction systems revealed the advantages of the thin film catalyst, which was immobilised directly on the photo-microreactor wall. The specific rate constant was more than 50 times higher in this arrangement for both model reactants. In addition, thin films of g-C_3N_4 were stable and well adherent during the microreactor tests with the repetitive reaction cycles. Plasma treatment considerably increased the hydrophilicity of the dried thin films, which resulted in their substantially higher photoactivity.

1. Introduction

Metal-free light-sensitive semiconductors are ranked among the promising solutions in the field of oxidative degradation of organic pollutants, organic synthesis of fine chemicals, and water splitting towards hydrogen [1,2]. Despite substantial efforts in the last 20 years, actual commercialisation of photocatalysts still requires further research and optimisations, as there is a lack of feasible, cheap, and robust materials also interacting with the visible part of the solar spectrum. Since the discovery of the photocatalytic activity of graphitic carbon nitride (g-C_3N_4) in 2006, this material has attracted considerable attention, but its history is much older [3,4]. It consists of tri-s-triazine rings cross-linked by trigonal N-atoms [2]. It is metal-free, with high thermal and chemical stability, a tuneable electronic structure, and it ranks among the medium-band-gap semiconductors. The electronic band gap of g-C_3N_4 is located around 2.7 eV, which is less than the electronic band gap of a photocatalytic standard, titanium dioxide (TiO_2), which is 3.2 eV [2]. From the electron structure, it is also apparent that the g-C_3N_4 should be capable of oxygen and hydrogen evolution by water splitting. Secondly, it is easy and inexpensive to synthesise, which also makes it attractive for larger-scale use. Carbon nitride exists in several allotropes, but the graphitic one is regarded as the most stable phase [1]. To date, g-C_3N_4 has already found application in wastewater purification [5], carbon dioxide storage [6], photochemical reduction [7] and hydrogen evolution [1,8]. Variations of g-C_3N_4 activity can be achieved by incorporating organic or inorganic compounds into the tri-s-triazine structure [2], or by modifying its morphology, i.e. g-C_3N_4 nanosheets and nanofibers [9,10]. To increase its performance in the photocatalytic

* Corresponding author.
E-mail address: vanluchene@icpf.cas.cz (A. Vanluchene).
[1] These authors contributed equally to this work.

https://doi.org/10.1016/j.jece.2022.108790
Received 19 April 2022; Received in revised form 3 October 2022; Accepted 14 October 2022
Available online 17 October 2022

process, it is desirable to choose and optimise the reaction system which is used. For instance, well-designed micro-flow reactors can intensify the process considerably, since the overall rate-determining step can be better controlled in comparison to batch reactor systems [11]. Photo-microreactor (PMR) systems with slit geometry usually reveal higher efficiency than batch photoreactors, as they offer higher heat and mass transfer capabilities, in particular easier light penetration into the whole reaction volume. Thus, the rate of mass-transfer limited reactions can be increased by lowering the dimensions of the reactor to the microscale [12]. Furthermore, the efficiency of the photochemical reactions is strongly dependent on the ability to use energy from the incident photons. Since the depth of the slit-geometry microreactors is short, the path for the light to penetrate the reaction mixture is also short, and therefore the reaction volume is irradiated more uniformly in contrast to the photochemistry performed in batch reactors [13,14]. In addition, photothermal catalysis can profit from photochemical microreactors, since the small reaction liquid volume can be heated up rapidly under the intensive light irradiation conditions [15,16]. In general, PMR is not a technology suitable for vast environmental cleanup, because of its low throughput which is problematic, e.g. for water purification. But it is the ideal technology to test and compare different thin films, since it provides a unique well-defined and precise system to evaluate the activity of thin films.

A common problem with microreactors is the risk of blockage of their small channels if larger solid phase particles are present. Therefore, the solid catalyst must be well-dispersed in a continuous phase. Typically formed aggregates of g-C_3N_4 should be smaller than tenths of micrometres. Another possibility is the catalyst immobilisation on the reactor's wall. This provides additional advantages, as no separation of the catalyst is needed. Thin films of carbon nitride can be prepared, for instance, by chemical vapour deposition (CVD) [17], liquid growth [18], or spin-coating [19]. Mazzati et al. prepared an ultrathin film of g-C_3N_4 (around 100 nm) by CVD method on lab vials and demonstrated higher activity of one order of magnitude of the thin film compared to the suspended particles for the oxidation of benzyl alcohols [17]. Safaei et al. prepared a thin film of g-C_3N_4 from ultrasonicated dispersion by spin-coating [20]. A thin film of TiO_2/g-C_3N_4 for the treatment of wastewater was fabricated by surface hybridisation and the dip-coating method [21]. Polymeric C_3N_4 was grown on different substrates by liquid-based evolution by Xu et al. [18]. Mohamed et al. [19] enhanced the electrochemical performance by γ radiation of spin-coated film of g-C_3N_4. Another possibility to enhance the performance of a spin-coated film of g-C_3N_4 is by post-annealing treatment. Mohamed et al. optimised the annealing temperature to achieve the lowest band gap and thus the best photocatalytic performance [22].

The activity of thin films can be influenced by plasma treatment [23], that is a widely used technique to improve the hydrophilic character by introducing hydrophilic functional groups [24]. For instance, Bu et al. achieved excellent hydrophilicity of C_3N_4 by oxygen plasma treatment [24]. Mao et al. [3] showed that, next to improved hydrophilicity, plasma treatment can exfoliate pristine g-C_3N_4 into an ultrathin nanosheet with increased surface area which leads to improvement of the photocatalytic performance. Lu et al. [25] used plasma-treated g-C_3N_4 to improve the photocatalytical H_2O_2 production.

To access the photoactivity of various photocatalysts, the photodegradation of Rhodamine B (RhB) is often employed. RhB is a fluorescent dye, used to stain biological specimens or animal vaccines. However, its extensive usage should be reduced due to its toxicity to aquatic systems and the fact that it possesses carcinogenic properties, as reported by recent research [26]. However, Rhodamine B is mostly a model system. This choice has a practical advantage, based on the simplicity of its concentration determination by spectrophotometry, due to its high photo-absorption (extinction) coefficient. For this reason, colour changes in the reaction mixture can be well measured even at very low concentrations. Rhodamine B is seen as an extensively used model dye, playing an undisputed role in the comparison of activities of similar photocatalysts prepared in different ways (if the rest of photocatalytic process parameters are kept constant). However, any generalisation of catalyst photoactivity results with RhB to other pollutants is limited and speculative, since too many parameters are involved [27]. Moreover, the actual quantum yield for a dye solution cannot be evaluated, since a dye always absorbs some of the light without necessarily photolysing it, thus light of lower intensity is then incident on the catalyst surface [28]. For these reasons, photodegradation experiments with the currently emerging wastewater pollutant, Tetracycline (TC), were also conducted in this work. TC is a broad-spectrum antibiotic, traceable in wastewater, and representing here a pollutant, of which the photodegradation mechanism has previously been well described [29].

In summary, here we report on a facile process to prepare functional and photoactive g-C_3N_4 thin films by the wet-coating method. Furthermore, we demonstrate the advantages of a combination of immobilised catalyst film deposited on the transparent microreactor wall for the photocatalytic degradation of two types of model pollutants: Rhodamine B and broad-spectrum antibiotic Tetracycline. The experimental algorithm was as follows: Synthesis of g-C_3N_4 was optimised for different calcination temperatures and its activity was tested in the batch. The catalyst particle size was decreased by wet ball milling and the photocatalytic activity of the milled catalyst was verified in the same reaction system. A thin film with an origin in the milled catalyst with a binder was prepared and tested in the photo-microreactor. Its photoactivity was further modified by post annealing and by low-temperature ambient-air plasma. Comparison of different reaction systems was evaluated and the advantages of a combination of thin film catalyst immobilised on the microreactor wall for photocatalysis were demonstrated. Furthermore, in comparison experiments of different reaction systems, we show a significant improvement of the photocatalytic process by using PMR, compared to the batch slurry reactor.

2. Materials and methods

These chemicals were used as received: melamine (Aldrich, 99%), cyanuric acid (Aldrich, 98%), chloroform (Lachner, p.a.), Rhodamine B (Aldrich, ≥ 95%), propan-2-ol (Merck, ≥ 99%), ethanol (Penta, ≥ 99%), α-terpineol (Aldrich, ≥ 95%), Tetracycline (Aldrich, 98–102% HPLC), $NaNO_2$ (Aldrich, ≥ 97%). Deionised water was filtered by Aqual 35 (Merci).

2.1. Synthesis of bulk g-C_3N_4

Graphitic C_3N_4 was prepared from a supramolecular complex from nitrogen rich precursors: melamine and cyanuric acid. These precursors create a supramolecular assembly through non-covalent interactions, resulting in graphitic-like structure and composition [30]. Briefly, precursors which are melamine (1.26 mg) in water (25 ml) and cyanuric acid (1.29 mg) in chloroform (25 ml) were mixed together in a shaker at 250 rpm for 4 h. At the interface of the two immiscible solvents, a supramolecular complex of white colour was observed. The solution was centrifuged at 3000 rpm for 10 min. The sediment was then dried in a furnace at 60 °C overnight to remove solvent residuals. Since the calcination temperature affects the g-C_3N_4 performance [31], the samples were then calcined in a covered alumina crucible in a furnace, for every sample at a different temperature level 350 °C, 450 °C, 550 °C, 650 °C for 4 h under a nitrogen atmosphere. The heating rate was 2.3 °C/min, after slow cooling to room temperature, the raw catalyst was collected. The typical yield of g-C_3N_4 was in the range from 10% to 14% (calculated from the weight of cyanuric acid and melamine).

To prepare a thin film of g-C_3N_4 immobilised on a glass surface, it was important to decrease the catalyst's size and enhance the particles' monodispersity. Thus, the catalyst was milled to achieve small, monodisperse particles. Wet ball milling was performed in a glass beaker with perpendicular vane stirrer made from chrome-plated stainless steel to minimise catalyst contamination during the milling. The lid over the

beaker, to prevent solvent evaporation, was custom-designed, cast from silicone rubber in a 3D-printed mould. Two glass rods were held by the lid in the mixing space to prevent tangential flow in the mill. Typically, 6 g of g-C_3N_4 was milled in 54 g of propan-2-ol (yielding 10 wt% dispersion) with 45 g of glass milling balls with diameter of 1 mm. Samples were milled at 850 rpm for 72 h. Once the milling was completed, the glass balls were separated on a nylon mesh. The prepared stock dispersion was used for analysis of the pure milled material and for the mixing of the coating formulation. An image of the milling setup, including all dimensions of the mill, can be found in the Supplementary Information (SI-1).

2.2. g-C_3N_4 photocatalyst characterisation

The structural characterisation of the supramolecular complex and g-C_3N_4 was performed by Fourier transform infrared spectroscopy (FTIR), using a Nicolet Avatar 360 spectrometer with ATR accessory (ZnSe crystal). Spectra were measured with 2 cm^{-1} resolution mode, in a spectral range from 400 to 4000 cm^{-1}.

The bulk g-C_3N_4 was characterised by X-ray diffraction (XRD) by a Bruker D8 Advance ECO diffractometer, equipped with LynxEye XE-T detector, with the X-ray source CuKα (0.15406 nm), 1000 W. The texture properties of g-C_3N_4 were evaluated, based on nitrogen adsorption isotherms, measured at 77 K by automated volumetric analysers (ASAP 2020 and ASAP 2050, Micromeritics, USA).

The elemental composition was determined by X-ray photoelectron spectroscopy (XPS) analysis, recorded on the ESCA 3400 photoelectron spectrometer, using Mg Kα radiation as the excitation source (1253.6 eV, energy 120 W). The samples were measured in a wide-scan mode 0 – 1000 eV (0.2 eV/step) and C1s, O 1 s and N 1 s spectra were measured in a high-resolution mode (0.05 eV/step). Samples were fixed on double-sided carbon tape. The thermal decomposition of the g-C_3N_4 precursor was evaluated by thermogravimetric analysis (TGA, Netzsch TG209 Libra). Measurements were performed in a temperature range of 20–800 °C under Ar, with temperature ramp 4 $K.min^{-1}$.

The g-C_3N_4 morphology was observed by scanning electron microscopy (SEM, Tescan Indusem scanning electron microscope equipped with a tungsten electron source and A65B secondary electron detector) and transmission electron microscopy (Jeol JEM-1010 TEM microscope).

Total reflectance UV–VIS spectra (i.e. diffuse plus specular) of the supramolecular complex and g-C_3N_4 was measured by the Specord 250 plus spectrophotometer by Analytic Jena (Germany), equipped with a 75 mm diameter integrating sphere working in the 8/d geometry. The recorded spectra were referenced against the manufacturer's provided Spectralon reflectance standard.

The energy band gap E_g was determined from Tauc plots, constructed with the use of the Tauc equation, where the absorption coefficient was replaced by the square root of the Kubelka-Munk function.

Particle size distribution to evaluate the effect of wet ball milling was determined by dynamic light scattering (DLS, HORIBA Partica LA-950 S2). The thin film of g-C_3N_4 was characterised by SEM imaging, and its hydrophilic/hydrophobic character by contact angel measurement (drop shape analyser DSA30, manufactured by Krüss GmbH, Germany). Images from the drop shape analysis can be found in the Supplementary Information (SI-4).

2.3. Preparation of g-C_3N_4 coatings

The coating formulation was prepared by mixing 6 ml of the milled 10 wt% stock g-C_3N_4 dispersion with 2 ml of 20 wt% ethanolic solution of polysiloxane dispersant/binder and 2 ml of α-terpineol. Details of the polysiloxane binder can be found in our previous communications [32,33], where it was employed for titanium oxide coatings. α-Terpineol acted as a viscosity modifier, and also prevented premature drying. Fused silica plates 78.8 mm × 36 mm with thickness of 6 ± 0.001 mm were used as substrates. The coating formulation was applied by a modified doctor blade technique. The substrate was covered by PET masking tape, 50 μm thick, into which the desired pattern to be coated was cut by an industrial laser cutter. The interior part of the patterned tape was lifted, and the exterior part served as a support of the doctor blade. Thus, a uniform film in the desired pattern was applied and its wet thickness was 50 μm. After drying, the thickness was reduced to 27 μm.

The thin film was modified to increase its hydrophilicity by atmospheric plasma discharge. Atmospheric-pressure, low-temperature ambient-air plasma was generated by a portable RPS40 plasma source (manufactured by Roplass Ltd., Czech Republic), equipped with a diffuse coplanar surface barrier discharge (DCSBD) plasma unit, which is essentially a dielectric barrier discharge (DBD) unit with a coplanar arrangement of the electrodes. The plasma discharge was powered by continuous-wave sinusoidal AC high voltage at a frequency of approx. 19 kHz. The total power input of 40 W yielded the volume power density of 160 $W.cm^{-3}$, which is the highest reported for ambient-air plasma generated by DBD. This was related to the unique configuration of the coplanar electrode setup, which enables the generation of a very thin film of surface plasma with a thickness of approximately 0.1–0.2 mm; there are therefore no losses due to the generation of plasma in the space where no material treatment is needed. Such "wasted plasma" is very typical of volume DBD, during which plasma is generated in the volume between the plane and cylindrical electrodes and the typical gap in open air is 1–3 mm. At the operational parameters employed for this work, the vibrational and rotational temperatures in plasma, determined by optical emission spectroscopy, were 2645 ± 195 K and 377 ± 18 K, respectively. The rotational temperature was calculated from the -OH band and may be interpreted as an upper limit for the neutral gas temperature in the plasma in the circumstances. The overall temperature of the gas is lower, and close to 70 °C. DCSBD is described in more detail in our previous communication [34,35].

It was also important here to focus on the effective fixation of the thin film on the glass surface, and its further modification. Stability of colloidal dispersion is generally influenced by particle size and by repulsive forces acting on the particles (electrostatic or steric stabilisation). Therefore, ethanol was used as a polar solvent, since it has a low boiling point (78 °C) and low surface tension (22 mN/m) and a proprietary polysiloxane stabiliser, acting also as a binder in the resulting dry film.

2.4. Batch reactor setup

A rectangular cuvette made from 3 mm thick quartz glass was used as a reference batch reactor. The cuvette dimensions (width x depth x height) were 36 × 20×52 mm and the irradiated volume was 25 ml. The cuvette was placed on an optical bench at a distance of 33.5 cm from the light source. The light source consisted of a mercury-xenon, 500 W compact lamp (Model 201–1 K, Safibra) with an infrared absorbing water filter. The light intensity was checked before and after each experiment, and was typically 23.4 $mW.cm^{-2}$. A 1 M solution of $NaNO_2$ in a rectangular cuvette inserted in the optical path was utilised as 400 nm cut-off UV filter in the case of the Tetracycline photodegradation. The optical spectrum of Hg(Xe) lamp with and without 400 nm cut-off filter can be found in the Supplementary Information (SI-2). The temperature of the reaction mixture was controlled by a thermocouple; temperature variation during the reaction was negligible. The proper mixing of the reaction solution in the batch reactor was ensured by a magnetic stirrer (IKA).

2.5. Photo-microreactor (PMR) setup

The photo-microreactor system consisted of the optical bench with the attached PMR at a distance of 33.5 cm from the light source, that was the same as for the batch reactor. The PMR (Ehrfeld Mikrotechnik BTS) was made from stainless steel (A4 1.4404). The irradiated reaction

volume 0.37 ml was defined by a 250 μm wide PFA (perfluoroalkoxyl) exchangeable spacer and a quartz cover mounted onto the reactor body. The quartz cover provided the irradiated area of 13.8 cm^2. A detailed outline description of PMR can be found in our previous publications [11,36]. The reactor was operated in a continuous loop, with a reaction mixture circulation (Fig. 1A). A peristaltic pump (Kouřil PCD81) with a flow rate of 63 $ml.min^{-1}$ through PMR was used. 25 ml of the reaction mixture was recirculated from a magnetically stirred storage beaker. The time of one cycle, the time needed to recirculate the whole reaction mixture through PMR, was 24 s. The PMR was cooled by pressurised air flowing through an integrated heat exchanger. The reaction temperature was measured by an integrated temperature sensor (Pt100). An optical flow cell for in-line absorbance measurement was placed into the reaction stream right behind the PMR. The reaction was performed under isothermal conditions at 25 °C. Important parameters, such as distance of the reactor from the irradiation source, light intensity, concentration and volume of the reaction mixture, reaction temperatures, were kept constant to ensure the comparability of both reactors (PMR and batch reactor). Parameters which could not be preserved in transition from batch reactor to PMR, i.e. irradiated area and amount of catalyst were well defined, and the kinetic constant was related to them.

2.6. Photocatalytic activity

The photocatalytic activity of bulk and immobilised g-C_3N_4 was evaluated in a model reaction, the degradation of a fluorescent dye Rhodamine B (RhB). In the case of the batch reactor, 25 mg of the g-C_3N_4 was dispersed in the 25 ml of aqueous solution of Rhodamine B (0.02 mM). In the case of the PMR, the same aqueous solution of Rhodamine B without the catalyst was used.

The activity of g-C_3N_4 thin film was examined by repeated reaction runs, between which the PMR was flushed by water for 20 min. No photocatalyst activation procedure was applied on fresh or used catalyst, nor between individual reaction cycles. To evaluate the reaction progress, reaction mixture samples of 500 μL were collected every 2 min, in the case of the cuvette. The centrifuge was further applied for removing the remaining catalyst (13 000 rpm, 10 min). The concentration of unreacted Rhodamine B was determined by UV–VIS spectrophotometer (Thermofisher Evolution 220; the calibration curve can be found in SI-6). In the case of PMR, absorbance of the sample was measured in the flow cell by in-line UV–VIS spectrometer (Ocean Optics) with interval of 10 s

In the case of Tetracycline (TC) degradation, the photocatalytic tests were performed in the same way as with Rhodamine B: 25 mg of the g-C_3N_4 was dispersed in 25 ml of aqueous solution of Tetracycline (50 mg/l). Photocatalytic degradation was evaluated by HPLC (Shimadzu HPLC instrument equipped with a UV detector set on 254 nm; the calibration curve can be found in SI-6). The column used for sample analysis was Hypersil Gold, 150x4.6 mm, 5 μm. 20 μL injected sample was eluted with 20 vol% acetonitrile and 80 vol% of 0.1 vol% acid trifluoroacetic and a buffered ultra-pure water solution. Elution flow was kept at 0.7 ml min^{-1} on low-pressure mode 7 MPa. The retention time of TC was 6.7 min. The samples were twice measured, and the results were presented as the decrease of the concentration of Tetracycline c normalised by initial Tetracycline concentration c_0.

3. Results and discussion

3.1. Structure and morphology of bulk g-C_3N_4

The supramolecular complex of melamine and cyanuric acid (CM complex) was prepared by mixing the two monomers in a 1:1 molar ratio in a water-chloroform solvent upon the appearance of the suspension. The formation of carbon nitride from the CM complex was confirmed by powder XRD (Fig. 2) and XPS (Fig. 3). The XRD patterns of the CM complex calcined at four different temperatures (350, 450, 550 and 650 °C) showed reflections at 10.7 and 27.8°2θ The wide reflection with a maximum at about 10.7°2θ belongs to a polymeric sample support (PMMA) and is not yet seen as relevant evidence for the g-C_3N_4 structure formation. The 28°2θ reflection appearing at 350 °C corresponds to a transition phase formed from the CM complex and disappears with increasing calcination temperature. The g-C_3N_4 typical reflection at 27.4°2θ (Fig. 2), which can be indexed as (002), is related to the interplanar stacking distance of graphitic carbon nitride films (d = 3.249 Å) and indicates a well-developed lamellar structure. For the temperature of 450 °C and higher, a phase is formed with maximum intensity at the 27.8°2θ (002) plane. From the g-C_3N_4 reference standard (PDF 00–063–0813, see Fig. 2), it is apparent that the highest intensity peak ascribed to the interplanar stacking distance typically occurs at

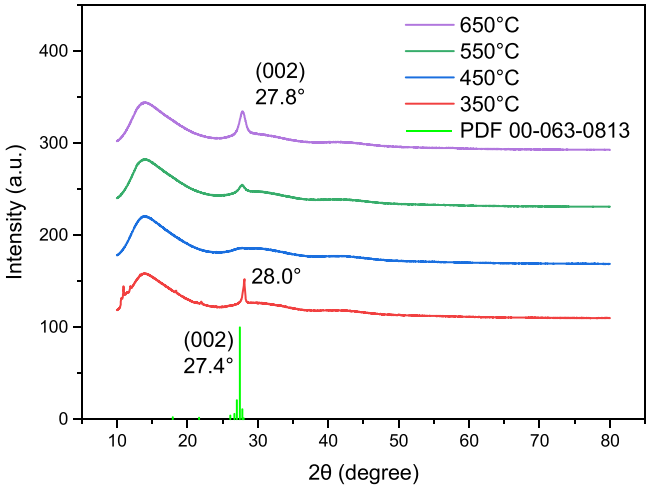

Fig. 2. XRD spectra of g-C_3N_4 calcined from supramolecular complex of melamine and cyanuric at different temperatures and stacking reflections of g-C_3N_4 (PDF 00–063–0813).

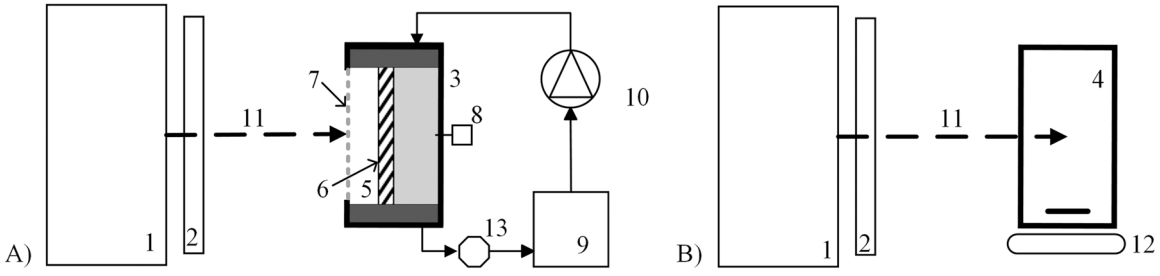

Fig. 1. Scheme of the A) PMR and B) batch reactor setup: (1) light source, (2) water filter, (3) PMR with temperature sensor (8) connected to the in-line absorbance measurement (13). Inside the PMR is placed glass slide (5) with a thin film of g-C_3N_4 (6). Light (11) penetrates through the slot (7) into the reaction space of the PMR and through the batch reactor (4) with a magnetic stirrer (12). Reaction mixture is pumped by peristaltic pump (10) from the reaction mixture reservoir (9).

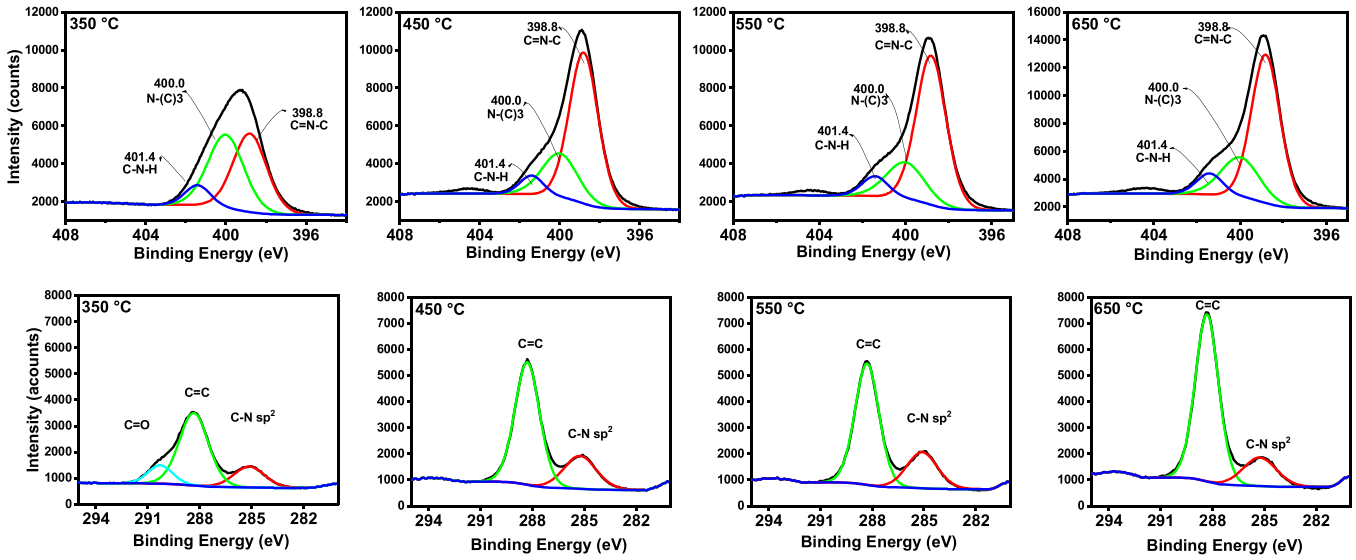

Fig. 3. N1s and C1s XPS spectra of g-C_3N_4 calcined at different temperatures.

27.4°2θ (002). This shift of the (002) reflection by 0.4°2θ is observed, which corresponds to the D-spacing d = 3.199 Å. Interestingly, the sample calcined at 450 °C appears to be the most amorphous, with minimal formation of layered g-C_3N_4 structure. Above this temperature, the lamellar character increases with the higher calcination temperature. Based on the Scherrer equation, we estimated the diffraction space size. The g-C_3N_4 calcined at 550 °C and 650 °C revealed a diffraction space size of 9 nm, and 12 nm, respectively.

The presence and interaction between the elements were evaluated from the high-resolution XPS analysis of individual N 1 s and C 1 s peaks (Fig. 3). The XPS spectra of g-C_3N_4 show a similar composition for all calcination temperatures, containing C, N, and a small amount of O, without the appearance of any other elements. From the nitrogen spectrum, the N 1 s can be divided into three peaks with maxima at 398.8 eV, 400.0 eV and 401.4 eV. The peaks at 400 eV and 401.4 eV can be assigned to the tertiary N-bonded atoms, N-(C)3 and C-N-H group, respectively. The peak at 398.8 eV represents the aromatic bond between N and C, thus the C═N-C structure. From the comparison of XPS spectra of g-C_3N_4 calcined at different temperatures, it is obvious that a fundamental transition is occurring between 350 °C and 450 °C, which correlates well with TGA results (Fig. 4). The atomic composition of g-C_3N_4 shows the oxygen content drop from 10.7% to 3.6% between these temperatures (see XPS atomic composition table SI-7). This oxygen release can be ascribed to the decomposition of the melamine-cyanuric acid complex. Oxygen content further decreases to reach 2.9% for calcination temperature 650 °C.

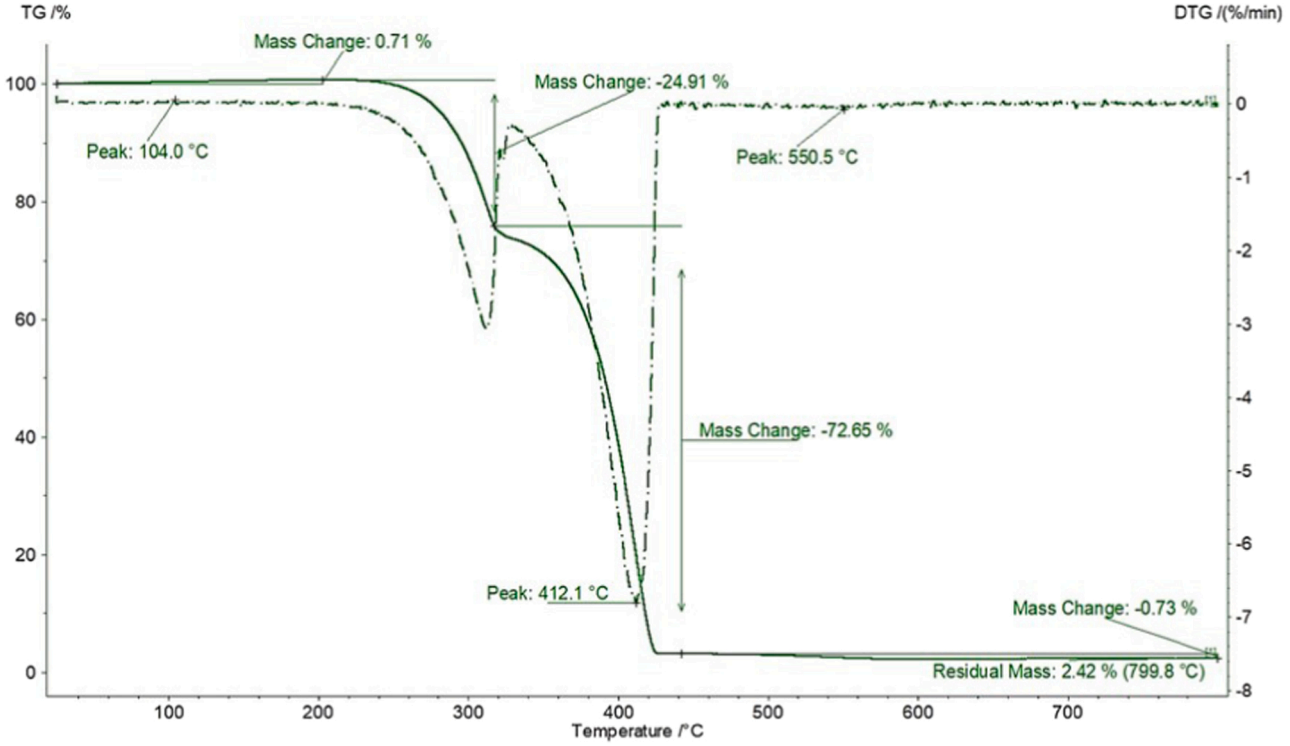

Fig. 4. TGA analysis of supramolecular complex of melamine and cyanuric acid.

Thermal decomposition of the CM complex was examined by TGA analysis (Fig. 4). The CM complex showed a weight loss (about 0.7%) at temperatures up to 200 °C, attributable to the withdrawal of physically adsorbed water due to the hydrophilic characteristic of the CM complex. The second stage at 300 °C exhibited a 25% mass change. In the range from 350 °C to 420 °C, a sharp decomposition process with 97% mass change was observed. Mass is then stable up to 550 °C; mass loss above 550 °C is assigned to the loss in the tri-s-triazine-based units.

The FT-IR spectra of the CM supramolecular complex and the g-C_3N_4 prepared at different calcination temperatures are presented in Fig. 5. The broad band at approximately 3390 cm^{-1} represents the -NH_2 stretching vibration in melamine; the band at 3230 cm^{-1} corresponds to the overlapping vibration of -OH groups or -NH groups of the cyanuric acid. The tertiary alcohol band at 1090 cm^{-1} of cyanuric acid (alcohol tautomeric form), -C-NH_2 vibration band at 1040 cm^{-1} together with both bands at 3380, 3220 cm^{-1} completely disappear at calcination temperatures of 450 °C and higher, which match the expected decomposition of the CM complex. Similarly, the 1780 and 1740 cm^{-1} corresponding to C═O groups of cyanuric acid (keto tautomeric form) also disappear. The last peaks disappearing with calcination at 1660 cm^{-1} represent deformation vibration of the -NH_2 groups and 766 cm^{-1} to the aromatic ring vibration of the melamine.

As the CM complex is being calcined, new peaks matching the chemical bonding between triazine building blocks of melamine and cyanuric acid appear. The absorption peak at 816 cm^{-1} is attributed to the characteristic breathing mode of the tri-s-triazine units. The bands at 1230, 1310, 1400 cm^{-1} (vibration modes of C-N) and 1540, 1630 cm^{-1} (vibration modes of C═N) are also typical for the g-C_3N_4 [37].

The specific surface area was evaluated from nitrogen adsorption isotherms in the range of relative pressures equal to $p/p_0 = 0.05–0.25$, using the standard Brunauer–Emmett–Teller (BET) procedure [38]. The values are summarised in Table 1, where S_{BET} denotes a specific surface area. S_{meso} is a specific surface area of mesopores and V_{micro} denotes a specific volume of micropores both evaluated by a *t*-plot method [39] based on Harkins & Jura master isotherm [40]. Finally, V_{tot} represents a total specific pore volume, evaluated from N_2 adsorption isotherm at relative pressure equal to $P/P_0 = 0.99$. The nitrogen sorption isotherms involving both adsorption and desorption branch for different calcination temperatures can be found in the Supplementary Information (SI-3). It follows from Table 1 that samples prepared at calcination temperatures of both 350 and 450 °C reveal similar textural characteristics, corresponding to the undeveloped inner pore structure (low values of S_{BET} as well as V_{tot}). On the other hand, above 450 °C, with increasing calcination temperature, both S_{BET} and V_{tot} increased significantly. However, predominant mesoporosity of the prepared samples (a typical low volume of micropores) is not affected by calcination temperature. The milled sample shows a higher specific surface area compared to the unmilled counterpart prepared at the same calcination temperature. In addition, by means of the milling process, the typical fraction of micropores disappeared (no volume of micropores was detected by the *t*-plot method).

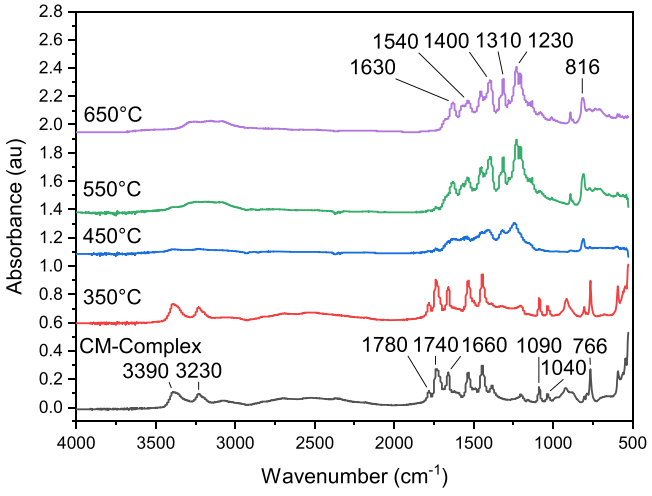

Fig. 5. FT-IR absorbance spectra of CM supramolecular complex, in comparison with g-C_3N_4 calcined at different temperatures.

The energy band gap (E_g) of g-C_3N_4 calcined at different temperatures was evaluated from Tauc plots (Fig. 6). E_g decreases with an increasing calcination temperature up to optimum at 550 °C. The lowest $E_g = 2.73$ eV was exhibited by the sample calcined at 550 °C, which agrees with the literature [41]. Increase in the energy band gap calcined at 650 °C can be accounted for by sample partial carbonisation.

3.2. *Effect of wet ball milling on g-C_3N_4 morphology*

The effect of ball milling on the particle size distribution of the g-C_3N_4 was evaluated by DLS measurement. The shift towards a lower average diameter and narrower size distribution was observed during the ball milling process. Fig. 7. A shows the vast effect of the ball milling on the decreasing size of the g-C_3N_4 particles. The crude g-C_3N_4 exhibited a broad size distribution, ranging from 1 to 100 μm with average diameter of about 31 μm. After 66 h, the particle size distribution became bimodal, with two main peaks corresponding to the diameters of 0.1 and 1 μm. This tremendous decrease was important for the ability to prepare a thin film of the catalyst. Note that the DLS method approximates the diameter of each particle as a diameter of a sphere, thus the size distribution must be interpreted carefully. In our case, the relative comparison of crude and milled samples was well possible. The specific surface area of milled g-C_3N_4 (67 $m^2.g^{-1}$) was comparable with the specific surface area of a raw material 55 $m^2.g^{-1}$. The milling process showed in fact almost no effect on the internal structure of the catalyst and the material remained mesoporous. Thus, during the milling processes, just the aggregates of the g-C_3N_4 were disintegrated, which led to the decrease of the particle size, while the internal structure remained virtually unchanged. These observations were also confirmed by SEM and TEM (Fig. 7).

3.3. *Characterisation of g-C_3N_4 thin films*

The thin film of g-C_3N_4 consisted of the milled g-C_3N_4 particles, as can be seen from SEM images in Fig. 8.B. The thickness of the thin film was evaluated from SEM (Fig. 8C), from a film cut positioned in the SEM chamber under the angle of $\alpha = 45°$ with respect to the point of view. The actual thickness of the thin film d was evaluated from measured distance x by trigonometry formula $d = x/(cos(\alpha))$. The measured distance x= 14 μm (Fig. 8C), hence the actual film thickness d was evaluated to be 27 μm. The surface of the film contained structural cracks developed during the post-annealing process. The surface wettability was examined by a contact angle measurement with the reaction mixture as a liquid phase (Rhodamine B solution). The surface tension of the water solution of Rhodamine B ($c = 0.02$ mM) was determined to be 64.4 $mN.m^{-1}$. The contact angles between the Rhodamine B solution and the catalyst film surface without and with a polysiloxane binder were 19° and 136°, respectively. Thus, the hydrophilic character of the film changed to highly hydrophobic in the presence of the binder. Although the hydrophobic nature can be seen as limiting regarding the intended application, this is not the case, as the binder is susceptible to further modifications and can be converted into the hydrophilic form by UV or by a subsequent plasma treatment [42]. Moreover, after the above-described process, the binder is almost completely mineralised into amorphous silica which is inert and stable. Therefore, the utilised binder is very suitable for photo- and electrocatalytic coatings, as it resists the corrosive attacks of reactive species generated in these systems. The presence of the binder was essential for the sufficient adhesion of the g-C_3N_4 catalyst film to the glass surface, otherwise the thin film

Table 1
Properties of g-C_3N_4 prepared at different calcination temperatures: textural characteristics; the energy band gap E_g; the kinetic constant k and the kinetic constant normalised by the specific surface k/S_{BET}.

T [°C]	S_{BET} [$m^2.g^{-1}$]	S_{meso} [$m^2.g^{-1}$]	V_{tot} [$mm^3_{liq}.g^{-1}$]	V_{micro} [$mm^3_{liq}.g^{-1}$]	E_g [eV]	k [min^{-1}]	k/S_{BET} [$min^{-1}.m^{-2}.g^1$]
350	7	6	24	< 1	2.95	0.03	0.0043
450	6	4	19	1	2.81	0.15	0.0250
550	56	44	208	7	2.73	0.19	0.0034
550 milled	67	–	295	–	–	0.29	0.0043
650	101	67	334	19	2.97	0.16	0.0016

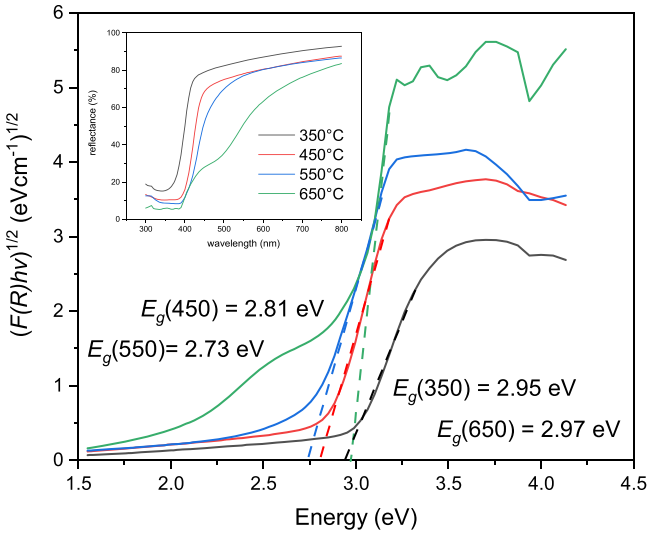

Fig. 6. UV–VIS reflectance and Tauc plots of g-C_3N_4 calcined at different temperatures.

would be washed out by the flow of the reaction mixture.

3.4. Photocatalytic degradation of Rhodamine B in the batch reactor

The photocatalytic activity of the prepared g-C_3N_4 was first evaluated by the degradation of RhB under polychromatic light irradiation. The light source was a mercury-xenon 500 W lamp with an infrared water filter. Prior to irradiation, the catalyst suspension in the RhB solution was stirred in the dark to reach adsorption-desorption equilibrium. The adsorption of Rhodamine B on the catalysts calcined at 350, 450, 550, and 650 °C resulted in its concentration decrease by 16%, 26%, 25%, and 34%, respectively (Fig. 9. B). The adsorption capacity increased with the higher calcination temperature, which correlated well with its increasing specific surface area. The highest adsorption, 34%, was observed for g-C_3N_4 calcined at 650 °C with surface area 101 m^2/g.

Fig. 9A shows the photocatalytic degradation of RhB for different g-C_3N_4 calcination temperatures. The RhB degradation by g-C_3N_4 after 10 min of irradiation was 20%, 74%, 83% and 78% for the calcination temperatures of 350, 450, 550 and 650 °C, respectively. Apparently, an optimum exists in the calcination temperature; the photocatalytic activity of the material increased with calcination temperature up to 550 °C. The degradation of RhB can be described by the pseudo-first order reaction model, thus the rate law is given by $r = -dC/dt = k*c$, from which it follows: $-ln(C/C_0) = k*t$, where C is actual concentration at the time t, C_0 is initial concentration and k is reaction rate constant. The evaluated reaction rate constants can be found in Table 1. The reaction rate constant was highest for the calcination temperature 550 °C. Milled g-C_3N_4 exhibited higher photocatalytic activity than the crude one ($k_{milled} = 0.29\ min^{-1}$ in comparison with $k_{crude} = 0.19\ min^{-1}$). Bigger aggregates of g-C_3N_4 were not as well dispersed in the reaction mixture as the smaller particles, and the smaller particles provide a much greater surface area that is accessible to the light. Average reaction rate constant and the standard deviation for g-C_3N_4 synthesised at 550 °C was $k = 0.26 \pm 0.07\ min^{-1}$ (Fig. 9. B). Fig. 10.

3.5. Photocatalytic degradation of Rhodamine B in the PMR

The photocatalytic activity of thin catalyst films was evaluated in the photo-microreactor (PMR). The rate constant in the microreactor was calculated based on the light exposure time t_{exp}. This accounts only for the time when the mixture was irradiated. The reaction mixture circulated throughout the microreactor setup, and it was exposed to the catalyst and irradiation only when it flowed through the slit geometry reaction chamber. Since the volume of the reaction chamber represented only a fraction with respect to the reaction mixture volume, the reaction time was corrected with respect to this volume ratio. The reaction chamber volume was $V_{reactor} = 0.372$ ml, total volume of the reaction mixture $V_{reaction\_mixture} = 25$ ml and the actual time of sample collection is t_{actual}, then the light exposure time $t_{exp}\ (PMR) = t_{actual} \cdot V_{reactor}/V_{reaction\_mixture}$. Naturally, in the cuvette, the exposure time $t_{exp}(Batch\ Reactor)$ is equal to the actual reaction time, since the whole reaction mixture volume is exposed to the catalyst and irradiation for the whole time of the experiment. The reaction mixture circulated for the first 10 min ($t_{exp}\ (PMR) = 0.15$ min) through the PMR in the dark to evaluate again the effect of Rhodamine B adsorption on the catalyst. This time was sufficient to reach the adsorption – desorption equilibrium and thus it was excluded in the evaluation of the kinetic constant (Fig. 11).

Based on previous experience [42], the fixation of a thin film of g-C_3N_4 with the binder (polysiloxane) on the glass was increased by sintering (annealing) it at 450 °C in N_2 atmosphere for 4 h. Nevertheless, the sintered thin film revealed very low photocatalytic activity ($k = 0.13\ min^{-1}$ see Table 2).

To improve thin film properties, the surface was treated by low-temperature ambient-air plasma to increase its wettability. The plasma treatment improved the hydrophilicity of the thin film significantly (contact angle decreased from 143° to 13°), as well as the photocatalytic performance ($k = 1.18\ min^{-1}$). The enhancement of degradation rate observed on the plasma-treated samples can be brought about by two simultaneously occurring phenomena. The first is the well-known effect of increased hydrophilicity of plasma-treated surfaces which facilitates wetting and adsorption of polar compounds [24]. The second is of a more complex nature and is related to the chemical modification of the catalyst surface. As the traditional solid-state synthesis of g-C_3N_4 results in a disorganised texture, with small grain size and irregular surface defects, poor charge separation and transfer ability inevitably occur. They then may limit its practical applications. Doping with heteroatoms may provide significant progress in the achievement of new electronic structures and morphologies of g-C_3N_4, as described in [43]; defect engineering and surface/interface engineering are very powerful tools for tuning the properties of g-C_3N_4 towards its development as a promising next-generation photocatalyst with excellent efficiency. The nitrogen defects in g-C_3N_4-x can generate mid-gap states, resulting in the up-shift of valance band and the downshift of conduction band. A suitable amount of mid-gap states can act as trapping sites for photo-generated carriers and thereafter deter their recombination,

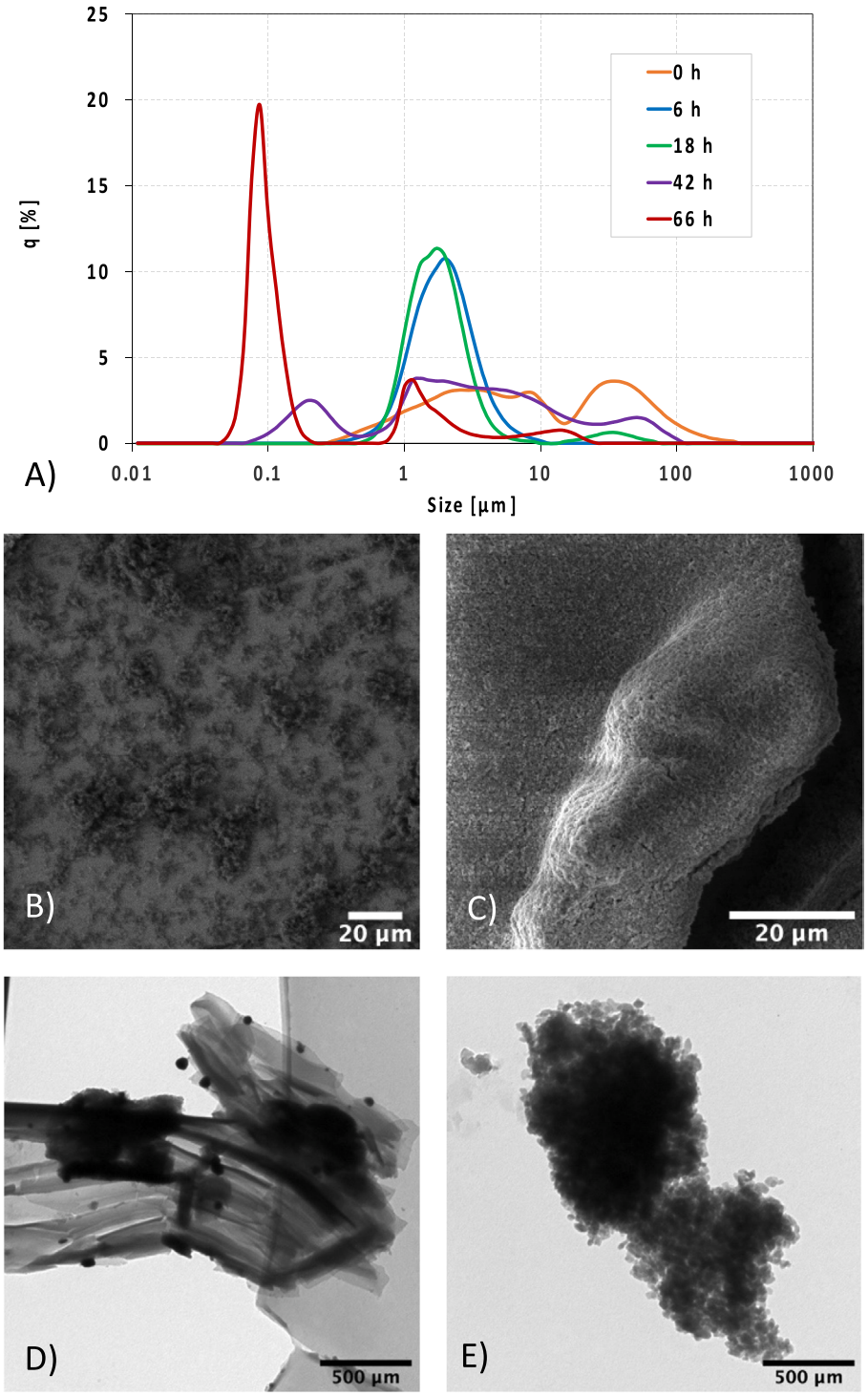

Fig. 7. A) Particle size distribution during the catalyst wet ball milling measured by DLS; SEM and TEM images of crude (B and D) and milled (C and E) catalyst.

consequently enhancing the overall quantum efficiency. Apparently, oxygen functionalisation induced by the plasma post-treatment seems to play a key role in reducing the recombination rate of the photoexcited charge carriers [44]. The exact nature and extent of plasma treatment on our layers goes well beyond the scope of this work, but its positive effect on the degradation kinetics is obvious and in good agreement with other published results.

In the case of skipping the annealing step (the thin film was only dried in the oven at 150 °C to remove the abundant solvent), the fixation of the thin film on the glass was still sufficient, but the photocatalytic performance was even higher ($k = 2.09\ \text{min}^{-1}$). The stability of the catalyst photoactivity is an important factor for practical use; therefore, several reaction cycles were applied with the same catalyst film (Fig. 11. B). A slight decrease in the photocatalytic activity of a dried thin film with the increasing number of cycles was observed (Table 3). To avoid this photoactivity decrease, the surface treatment by low-temperature ambient-air plasma was also proven as efficient. According to the results, the plasma treatment of the surface resulted in the increased stability of the thin film. In addition, the plasma-treated surface exhibited good activity, even after three weeks of standby; the thin film exhibited

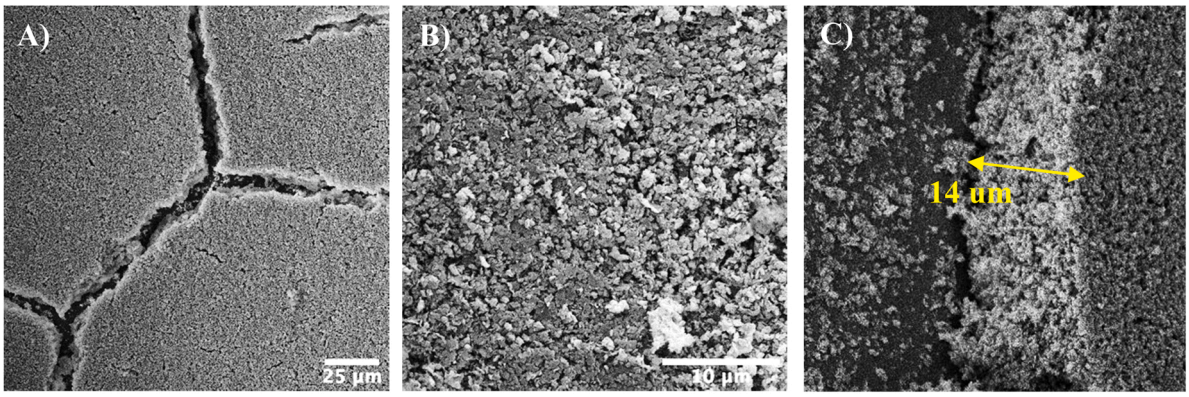

Fig. 8. SEM images of g-C_3N_4 thin films. A) Thin film defects; B) Structure of the thin film; C) 45° angle view of the thin film thickness d = 14/(cos(45°)) = 27 µm.

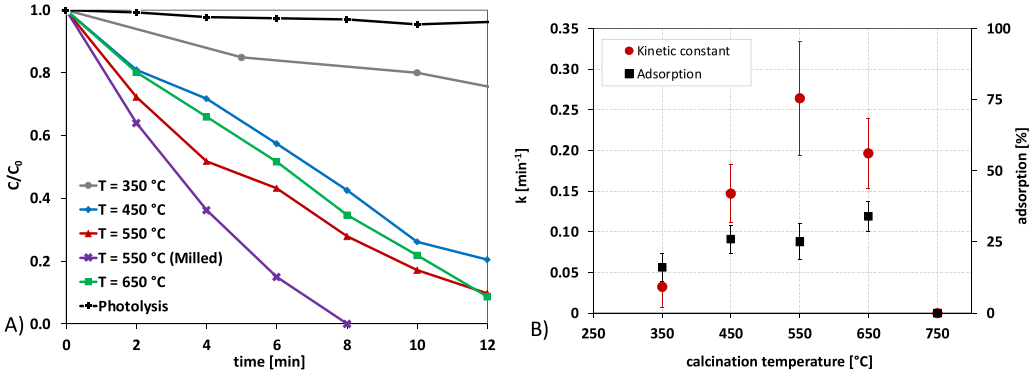

Fig. 9. A) Photocatalytic activity of g-C_3N_4 calcined at different temperatures; B) Kinetic constant and adsorption rate of Rhodamine B on the catalyst at different calcination temperatures.

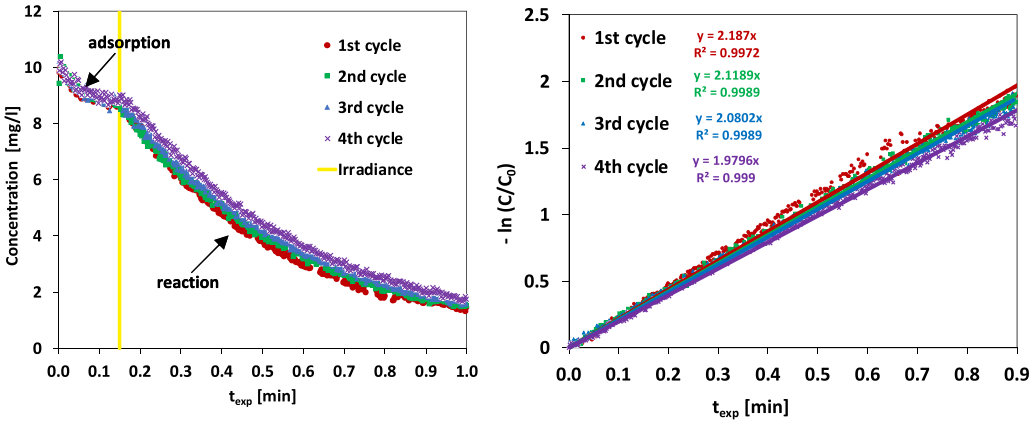

Fig. 10. Photocatalytic activity of thin film of g-C_3N_4 dried in the oven without any further modification in PMR: A) Concentration profile for adsorption and reaction; B) Kinetic fitting for the degradation of Rhodamine B under irradiation.

the same catalytic performance in six repeated cycles (Table 3).

Table 4 shows the comparison of three different reactor systems based on the same g-C_3N_4 type: (i) catalyst dispersed in the reaction mixture and stirred in the cuvette, i.e. batch slurry photocatalysis (ii) catalyst dispersed in the reaction mixture and circulating through the PMR, i.e. continuous slurry photocatalysis and (iii) catalyst immobilised as a thin film (dried and plasma-treated) on a transparent PMR wall, i.e. flow photocatalysis with immobilised catalyst. Note that the reactors were operated under the same irradiance conditions (see part 2.4). All the reaction systems can be compared by specific rate constant k^*, that is related to the weight of catalyst m and light exposure area A. The specific rate constant k^* was more than 50 times higher in the microreactor with g-C_3N_4 thin film than in the cuvette, which indicates 50 times faster degradation of Rhodamine B. The specific rate constant is also higher for the immobilised catalyst, compared to the reaction system with a catalyst suspension in the microreactor (21 $min^{-1}.cm^{-2}.g^{-1}$ in suspension, in comparison with 41 $min^{-1}.cm^{-2}.g^{-1}$ when immobilised).

3.6. Photocatalytic degradation of Tetracycline

Next, photocatalytic activity of the produced samples was also tested with Tetracycline (TC). Experiments were conducted in the same way as

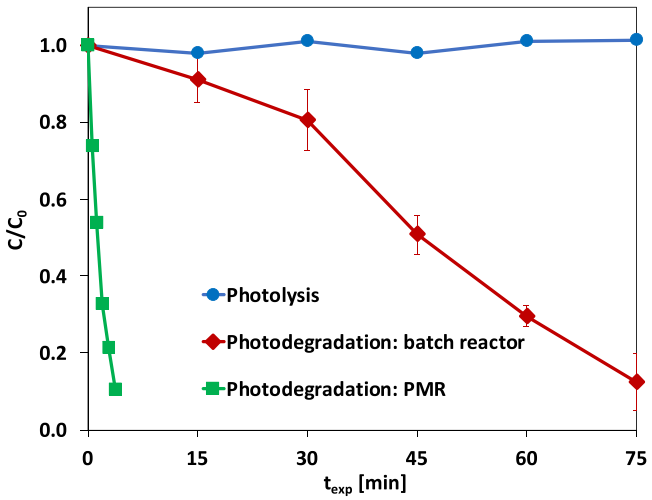

Fig. 11. Tetracycline photodegradation in the batch reactor and PMR.

Table 2
Kinetic constants for thin film of g-C_3N_4 with different surface modification.

Description of thin film	k [min^{-1}]
Sintered 450 °C	0.13
Sintered 450 °C + plasma	1.18 ± 0.11
Dried	2.09 ± 0.07
Dried + plasma	2.62 ± 0.03
Dried + plasma + 21 days	2.30 ± 0.17

Table 3
Kinetic properties of thin film for several reaction cycles.

Description of thin film	Dried	Dried + Plasma	Dried + Plasma (21 days)
Cycle number	***k*** **[min^{-1}]**	***k*** **[min^{-1}]**	***k*** **[min^{-1}]**
1	2.19	2.34	2.52
2	2.12	2.74	2.30
3	2.08	2.69	2.34
4	1.98	2.71	2.03
5	–	–	2.46
6	–	–	2.44

Table 4
Comparison of different reactor systems.

	k [min^{-1}]	A [cm^2]	m [mg]	k/m [$min^{-1}.g^{-1}$]	k^* [$min^{-1}.cm^{-2}.g^{-1}$]
Batch reactor g-C_3N_4 suspension	0.36	17.7	25	14	0.8
PMR g-C_3N_4 suspension	6.85	13.2	25	274	21
PMR g-C_3N_4 thin film	2.62	13.2	4.9	535	41

for Rhodamine B, with the only difference that the cut-off filter under 400 nm was used to minimise the photolysis and the reaction was carried for a longer period of time. Before starting, the reaction mixture with g-C_3N_4 was left in the dark for 15 min to reach the adsorption equilibrium.

The adsorption of TC on the catalyst resulted in its concentration decrease by 25%. The conversion of TC in the presence of g-C_3N_4 was 87% after 75 min of the reaction and the photolysis (photodegradation without the presence of g-C_3N_4) was negligible at the same time (Fig. 11). To identify the reaction intermediates, the samples were analysed by HPLC-MS. Complete degradation of TC in the presence of g-C_3N_4 was already published by Fattahimoghaddam et al. [45]. Photocatalytic degradation of TC was also evaluated in the PMR to test the activity of the thin layer of g-C_3N_4. For this purpose, the thin film dried in the oven with no plasma treatment was used. The TC degradation in PMR was performed under the same conditions as in the case of Rhodamine B, except for the < 400 nm cut-off filter ($NaNO_2$ solution) positioned in front of the reactor. During the TC degradation in the PMR, the HPLC-MS determined compounds exhibited $m/z = 445.7$ that is the mass of TC followed mainly the degradation intermediates with $m/z = 431$. The TC degradation proceeded in the same pathway as suggested by Fattahimoghaddam et al. [45]. The degradation of TC in the batch reactor and in the PMR can be compared by specific rate constant k^*, that is related to the weight of catalyst m and light exposure area A, which were the same as in the photodegradation of Rhodamine B (Table 4). The specific rate constant k^* was 175 times higher in the PMR with g-C_3N_4 thin film than in the cuvette (Table 5), which indicates a vast improvement in the photodegradation process.

4. Conclusion

Graphitic carbon nitride was synthesised from a supramolecular complex of melamine and cyanuric acid and calcined at different temperatures. The g-C_3N_4 calcined at 550 °C revealed the best photocatalytic activity for the photodegradation of Rhodamine B. The mean size of g-C_3N_4 microparticles decreased by wet ball milling from 31 μm to 1 μm. The milled g-C_3N_4 exhibited slightly higher catalytic activity than the crude one, specifically the reaction rate constant increased from 0.19 min^{-1} to 0.29 min^{-1}. A thin film of milled g-C_3N_4 was prepared on a glass slide with polysiloxane as a binder. The effect of the post-processing treatment of the thin film on its photocatalytic activity was studied. The g-C_3N_4 thin film dried at 150 °C exhibited a higher photocatalytic activity in comparison with the samples sintered at 450 °C. Surface modification by plasma treatment increased the overall time stability of the thin film and its reusability; in six repeated reaction cycles, no decrease in photocatalytic activity was observed. Different reactor systems were compared by means of specific rate constant k^* related to the irradiated area and weight of the catalyst. The modified reaction rate constant for the photo-microreactor with a g-C_3N_4 thin film was 50 times higher in comparison with the batch reactor with the g-C_3N_4 dispersed in the reaction mixture. The almost 2x improvement (k^* increased from 21 to 41 min^{-1}) was observed with the immobilised thin film catalyst compared to the dispersed catalyst, both examined in the photo-microreactor under flow conditions. The photocatalytic activity of g-C_3N_4 to catalyse photodegradation of Tetracycline antibiotic was also evaluated. The conversion of Tetracycline reached 87% after 75 min; the photolysis of TC was negligible. Degradation of TC in the photo-microreactor with a thin layer of g-C_3N_4 showed about 175x higher kinetic constant compared to the batch reactor (k^* increased from 0.05 to 8.58 min^{-1}), indicating a vast improvement in the photodegradation process efficiency.

In summary, the synergic effect of the combination of a photo-microreactor and a catalyst thin film was proven by the increased photocatalytic performance. This is virtually the first study on g-C_3N_4 thin films tested for their photocatalytic activity in the photo-microreactor [11,46,47]. Implementation of the highly photoactive

Table 5
Comparison of Tetracycline degradation in the batch reactor and PMR.

	k [min^{-1}]	k/m [$min^{-1}.g^{-1}$]	k^* [$min^{-1}.cm^{-2}.g^{-1}$]
Batch reactor g-C_3N_4 suspension	0.02	0.87	0.05
PMR g-C_3N_4 thin film	0.56	113	8.58

thin film on a transparent reactor wall, that is irradiated from one side and in contact with the reaction media from the other side, is an easily scaled-up solution with high potential for many practical applications.

Subsequent research will focus on the surface modification of thin films (post annealing, different plasma treatment or g-C_3N_4 doping) to further enhance the photocatalytic activity of g-C_3N_4 thin films.

CRediT authorship contribution statement

Susmita Dolai: Synthesis of g-C3N4 and experiments in the batch reactor, **Anna Vanluchene:** Photo-microreactor experiments, Writing, Reviewing and Editing, **Petr Dzik:** Milling of g-C3N4 and preparation of the thin layers, **Radek Fajgar, Karel Soukup:** Analysis of g-C3N4 (FT-IR, XPS, XRD, SEM, BET), **Petr Stavárek and Petr Klusoň:** Writing, Reviewing and Editing.

Declaration of Competing Interest

The authors declare that they have no known competing financial interests or personal relationships that could have appeared to influence the work reported in this paper.

Data availability

Data will be made available on request.

Acknowledgement

This research was financially supported by the Technology Agency of the Czech Republic (project No. SS02030008, programme: Environment for Life).

Appendix A. Supporting information

Supplementary data associated with this article can be found in the online version at doi:10.1016/j.jece.2022.108790.

References

[1] X.C. Wang, et al., A metal-free polymeric photocatalyst for hydrogen production from water under visible light, Nat. Mater. 8 (1) (2009) 76–80.
[2] X.C. Wang, S. Blechert, M. Antonietti, Polymeric graphitic carbon nitride for heterogeneous photocatalysis, ACS Catal. 2 (8) (2012) 1596–1606.
[3] F. Goettmann, et al., Chemical synthesis of mesoporous carbon nitrides using hard templates and their use as a metal-free catalyst for friedel-crafts reaction of benzene, Angew. Chem. -Int. Ed. 45 (27) (2006) 4467–4471.
[4] F. Goettmann, et al., Metal-free catalysis of sustainable Friedel-Crafts reactions: direct activation of benzene by carbon nitrides to avoid the use of metal chlorides and halogenated compounds, Chem. Commun. (43) (2006) 4530–4532.
[5] E. Haque, et al., Superior adsorption capacity of mesoporous carbon nitride with basic CN framework for phenol, J. Mater. Chem. 20 (48) (2010) 10801–10803.
[6] Q. Li, et al., *Facile synthesis of porous carbon nitride spheres with hierarchical three-dimensional mesostructures for CO_2 capture*, Nano Res. 3 (9) (2010) 632–642.
[7] J.L. Lin, Z.M. Pan, X.C. Wang, Photochemical Reduction of CO_2 by Graphitic Carbon Nitride Polymers, Acs Sustain. Chem. Eng. 2 (3) (2014) 353–358.
[8] R. Shwetharani, et al., Photocatalytic semiconductor thin films for hydrogen production and environmental applications, Int. J. Hydrog. Energy 45 (36) (2020) 18289–18308.
[9] Q. Han, et al., Graphitic carbon nitride/nitrogen-rich carbon nanofibers: highly efficient photocatalytic hydrogen evolution without cocatalysts, Angew. Chem. -Int. Ed. 55 (36) (2016) 10849–10853.
[10] X.H. Wu, et al., Soluble g-C3N4 nanosheets: Facile synthesis and application in photocatalytic hydrogen evolution, Appl. Catal. B-Environ. 247 (2019) 70–77.
[11] S. Hejda, et al., Microreactor as efficient tool for light induced oxidation reactions, Chem. Eng. J. 255 (2014) 178–184.
[12] R.L. Hartman, J.P. McMullen, K.F. Jensen, Deciding Whether To Go with the Flow: Evaluating the Merits of Flow Reactors for Synthesis, Angew. Chem. -Int. Ed. 50 (33) (2011) 7502–7519.
[13] M. Liu, et al., Tube-in-tube hollow fiber catalytic membrane microreactor for the hydrogenation of nitrobenzene, Chem. Eng. J. 354 (2018) 35–41.
[14] A. Yusuf, C. Garlisi, G. Palmisano, Overview on microfluidic reactors in photocatalysis: Applications of graphene derivatives, Catal. Today 315 (2018) 79–92.
[15] Y.K. Chen, et al., Photothermal effect enhanced photocatalysis realized by photonic crystal and microreactor, Appl. Surf. Sci. (2020) 534.
[16] K.S. Elvira, et al., *The past*, present and potential for microfluidic reactor technology in chemical synthesis, Nat. Chem. 5 (11) (2013) 905–915.
[17] S. Mazzanti, et al., Carbon Nitride Thin Films as All-In-One Technology for Photocatalysis, ACS Catal. 11 (17) (2021) 11109–11116.
[18] J.S. Xu, et al., Liquid-based growth of polymeric carbon nitride layers and their use in a mesostructured polymer solar cell with V-oc exceeding 1 V, J. Am. Chem. Soc. 136 (39) (2014) 13486–13489.
[19] N.A. Mohamed, et al., Efficient Photoelectrochemical Performance of gamma Irradiated g-C3N4 and Its g-C3N4@BiVO4 Heterojunction for Solar Water Splitting, J. Phys. Chem. C. 123 (14) (2019) 9013–9026.
[20] J. Safaei, et al., Facile fabrication of graphitic carbon nitride, (g-C3N4) thin film, J. Alloy. Compd. 769 (2018) 130–135.
[21] Z. Wei, et al., Photoelectrocatalytic degradation of phenol-containing wastewater by TiO2/g-C3N4 hybrid heterostructure thin film, Appl. Catal. B-Environ. 201 (2017) 600–606.
[22] N.A. Mohamed, et al., The influences of post-annealing temperatures on fabrication graphitic carbon nitride, (g-C3N4) thin film, Appl. Surf. Sci. 489 (2019) 92–100.
[23] C.K. Jung, et al., Plasma surface modification of TiO2 photocatalysts for improvement of catalytic efficiency, Surf. Coat. Technol. 200 (5–6) (2005) 1320–1324.
[24] X.M. Bu, et al., Surface Modification of C3N4 through Oxygen-Plasma Treatment: A Simple Way toward Excellent Hydrophilicity, Acs Appl. Mater. Interfaces 8 (45) (2016) 31419–31425.
[25] N. Lu, et al., Characterization of highly effective plasma-treated g-C3N4 and application to the photocatalytic H2O2 production, Chemosphere (2020) 241.
[26] M.S. Tahir H, m *Using dyes to evaluate the photocatalytic activity*. Interface Science and Technology, Elsevier,, 2021.
[27] P. Kluson, et al., Is It Possible to Compare Activities of Heterogeneous Photocatalysts in Aqueous Phase? Chem. Listy 105 (10) (2011) 738–744.
[28] B. Ohtani, Photocatalysis A to Z-What we know and what we do not know in a scientific sense, J. Photochem. Photobiol. C. -Photochem. Rev. 11 (4) (2010) 157–178.
[29] C. Reyes, et al., Degradation and inactivation of tetracycline by TiO2 photocatalysis, J. Photochem. Photobiol. a-Chem. 184 (1–2) (2006) 141–146.
[30] Dolai, S., et al., *Solvent-Assisted Synthesis of Supramolecular-Assembled Graphitic Carbon Nitride for Visible Light Induced Hydrogen Evolution - A Review.* Chemcatchem, 2021.
[31] Z. Mo, et al., Synthesis of g-C3N4 at different temperatures for superior visible/UV photocatalytic performance and photoelectrochemical sensing of MB solution, Rsc Adv. 5 (123) (2015) 101552–101562.
[32] M. Kralova, et al., Cold-setting inkjet printed titania patterns reinforced by organosilicate binder, Molecules 20 (9) (2015) 16582–16603.
[33] T. Svoboda, et al., Low-temperature mineralisation of titania-siloxane composite layers, Catalysts 11 (1) (2021).
[34] M. Cernak, et al., Diffuse Coplanar Surface Barrier Discharge and its applications for in-line processing of low-added-value materials, Eur. Phys. J. -Appl. Phys. 47 (2)) (2009).
[35] T. Homola, et al., Plasma treatment of glass surfaces using diffuse coplanar surface barrier discharge in ambient air, Plasma Chem. Plasma Process. 33 (5) (2013) 881–894.
[36] Z. Vajglova, et al., Photochemical degradation of polybrominated diphenyl ethers in microreactor, Res. Chem. Intermed. 41 (12) (2015) 9373–9381.
[37] M. Kim, S. Hwang, J.S. Yu, Novel ordered nanoporous graphitic C3N4 as a support for Pt-Ru anode catalyst in direct methanol fuel cell, J. Mater. Chem. 17 (17) (2007) 1656–1659.
[38] L.S.D. Stephen Brunauer, Deming W.Edwards, Teller Edward, On a theory of the van der Waals adsorption of gases, J. Am. Chem. Soc. 62 (7) (1940) 1723–1732.
[39] J.H. Deboer, et al., T-Curve of Multimolecular N2-Adsorption, J. Colloid Interface Sci. 21 (4) (1966), 405-&.
[40] G. Jura, W.D. Harkins, Surfaces of Solids.14. A Unitary Thermodynamic Theory of the Adsorption of Vapors on Solids and of Insoluble Films on Liquid Subphases, J. Am. Chem. Soc. 68 (10) (1946) 1941–1952.
[41] A. Alaghmandfard, K. Ghandi, A Comprehensive Review of Graphitic Carbon Nitride (g-C3N4)-Metal Oxide-Based Nanocomposites: Potential for Photocatalysis and Sensing, Nanomaterials 12 (2) (2022).
[42] P. Dzik, et al., The influence of curing methods on the physico-chemical properties of printed mesoporous titania patterns reinforced by methylsilica binder, Catal. Today 313 (2018) 26–32.
[43] A. Kumar, et al., C-, N-Vacancy defect engineered polymeric carbon nitride towards photocatalysis: viewpoints and challenges, J. Mater. Chem. A 9 (1) (2021) 111–153.
[44] X.G. Ji, et al., Tuning the photocatalytic activity of graphitic carbon nitride by plasma-based surface modification, Acs Appl. Mater. Interfaces 9 (29) (2017) 24616–24624.
[45] H. Fattahimoghaddam, T. Mahvelati-Shamsabadi, B.K. Lee, Efficient Photodegradation of Rhodamine B and Tetracycline over Robust and Green g-C3N4 Nanostructures: Supramolecular Design, J. Hazard. Mater. (2021) 403.
[46] N. Wang, et al., Microfluidic photoelectrocatalytic reactors for water purification with an integrated visible-light source, Lab a Chip 12 (20) (2012) 3983–3990.
[47] M. Krivec, et al., Highly Efficient TiO2-Based Microreactor for Photocatalytic Applications, Acs Appl. Mater. Interfaces 5 (18) (2013) 9088–9094.